

A pressure-free long-time stable reduced-order model for two-dimensional Rayleigh-Bénard convection

K. Chand^a, H. Rosenberger^a, B. Sande^a

^aCentrum Wiskunde & Informatica, Science Park 123, Amsterdam, The Netherlands

Abstract

The present work presents a stable POD-Galerkin based reduced-order model (ROM) for two-dimensional Rayleigh-Bénard convection in a square geometry for three Rayleigh numbers: 10^4 (steady state), 3×10^5 (periodic), and 6×10^6 (chaotic). Stability is obtained through a particular (staggered-grid) FOM discretization that leads to a ROM that is pressure-free and has skew-symmetric (energy-conserving) convective terms. This yields long-time stable solutions without requiring stabilizing mechanisms, even outside the training data range. The ROM's stability is validated for the different test cases by investigating the Nusselt and Reynolds number time series and the mean and variance of the vertical temperature profile. In general, these quantities converge to the FOM when increasing the number of modes convergence, and turn out to be a good measure of accuracy for the non-chaotic cases. However, for the chaotic case, convergence with increasing numbers of modes is not evident, and additional measures are required to represent the effect of the smallest (neglected) scales.

1. Introduction

Rayleigh-Bénard convection (RBC) is an idealized system to study natural thermal convection [1, 2]. Natural convection is ubiquitous in nature and has applications in geophysical aspects, astronomy, and inside the planets, to name a few [3, 4]. RBC is a bottom-heated and top-cooled configuration, where the flow is set in motion due to thermo-convective instabilities which arise from the thermal expansion of the working fluid. While the buoyant force destabilizes the flow (due to thermal expansion), viscous forces act as a stabilizing agent. The ratio of buoyant force to viscous force is known as the Rayleigh number $Ra = g\beta\Delta TH^3/(\nu\alpha)$. Here, g is the acceleration due to gravity, β is the thermal expansion coefficient, $\Delta T (= T_H - T_C)$ is the temperature difference between the two isothermal plates separated by a height H , and ν and α are the viscous and thermal diffusivities, respectively. Next to the Rayleigh number, the Prandtl number ($Pr = \nu/\alpha$) is another control parameter (which is a fluid property).

For a fixed working fluid and geometry (aspect ratio), finding the dependence of the heat flux (Nusselt number, Nu) and the flow intensity (Reynolds number, Re) on the Rayleigh number are the two key issues in RBC [5, 6]. A number of theories were proposed to establish these dependencies, namely, the classical 1/3 scaling [7], the ultimate regime in turbulent convection [8], and the unified scaling theory [9]. To ascertain the evidence of the existing theories and to develop new ones, a sufficiently large temporal sample of Nu and Re is required in order to compute averages and statistics. In addition to Nu and Re , several other quantities that are of interest require simulating large time intervals. For instance, the time-average temperature field is of interest as it quantifies the mean thermal boundary layer thickness [3, 10, 11] and the structure function reveals the small-scale dynamics [12]. Furthermore, investigation of large-scale circulation and flow reversals require a large sampling interval (more than 10^4 non-dimensional time units) [13]. Similarly, thermal plumes are quantified by averaging the fluctuations of vertical velocity and temperature over sufficiently large time span [14, 11]. Lastly, identification of turbulent super-structures has recently gained momentum, which are quantified by the mean temperature field [15, 16]. All these studies indicate the importance of long time-sampling in turbulent Rayleigh-Bénard convection.

In numerical experiments, turbulent flows are simulated by direct numerical simulation (DNS), large-eddy simulation (LES) and Reynolds-averaged Navier-Stokes techniques (RANS), see [17] for more details. For use

in optimization, design, control and uncertainty quantification studies, such simulations are typically computationally too expensive, and reduced-order model (ROM) can be advantageous. There are several different ROM approaches, for instance, proper orthogonal decomposition (POD)-Galerkin methods, Krylov subspace methods, and balanced truncation [18, 19]. In the present work, we use a POD-Galerkin based ROM, where the solution is expanded in terms of POD modes and the governing equations of the full-order model (FOM) are projected onto a lower-dimensional space (the so-called Galerkin step). The lower-dimensional space is constructed from the instantaneous snapshots of the FOM.

It has been observed that projection-based methods work appropriately for diffusion-dominated systems, owing to the sharp decay of the singular values of the snapshot matrix [19]. In such systems, neglecting the higher modes (associated to smallest length scales, which contain little energy), makes the POD-based ROMs efficient. On the contrary, for convection-dominated problems like turbulent flows, kinetic energy dissipation occurs at the smallest length scale (Kolmogorov length scale). In this case, discarding the highest modes results in the incorrect dissipation rate in ROMs, which can make them inaccurate and/or unstable. In addition, another stability issue that can potentially arise is due to the inf-sup condition (compatibility between pressure and velocity spaces), which needs to be satisfied at the ROM level [20].

Several different methodologies have been used to tackle these stability issues, for instance, using closure models to include the dissipation [21, 22, 23] or using a H^1 norm instead of l^2 norm to construct a POD basis [24]. Structure preservation is another way to handle the stability issues [25, 26]. In a recent study, [26] proposed a structure-preserving (kinetic energy-conserving) non-linearly stable reduced-order model for incompressible flows. The main idea behind the stable formulation was to discretize and project the governing equations in such a way that important symmetries of the incompressible Navier-Stokes equations are kept on the ROM level, leading to exact kinetic energy conservation (in the inviscid limit) and hence stability. This methodology was implemented for isothermal flows. In this work, this energy-stable ROM is extended to non-isothermal flow, allowing us to achieve the main goal of this article: *perform long-time sampling with a ROM for a thermal convection problem*. Although this approach does not directly solve the issue of representing the smallest scales and associated dissipation, the stable nature of the model makes it an excellent starting point for closure model development aimed at accuracy, without being concerned about stability.

The paper is organized as follows. In Section 2, the governing equations and the numerical details of the FOM is described. Section 3 encompasses the formulation of the ROM. In Section 4, stability and accuracy of the ROM are shown for three cases: steady flow 4.1; periodic flow 4.2; and chaotic flow 4.3. Finally, the paper is summarized in Section 5.

2. Full-order model description

2.1. Mathematical modeling

Rayleigh-Bénard convection is a buoyancy-driven flow governed by the mass, momentum, and energy equations. It can be considered as incompressible flow by invoking the Boussinesq approximation, which allows to incorporate density variation in the body force term. The governing equations can be written in their non-dimensionalized form as:

$$\nabla \cdot \mathbf{u} = 0, \quad (1)$$

$$\frac{\partial \mathbf{u}}{\partial t} + \nabla \cdot (\mathbf{u} \otimes \mathbf{u}) = -\nabla p + \sqrt{\frac{\text{Pr}}{\text{Ra}}} \nabla \cdot (\nabla \mathbf{u} + (\nabla \mathbf{u})^T) + \theta \hat{\mathbf{e}}_y, \quad (2)$$

$$\frac{\partial \theta}{\partial t} + \nabla \cdot (\mathbf{u} \theta) = \frac{1}{\sqrt{\text{PrRa}}} \nabla^2 \theta. \quad (3)$$

Here $\hat{\mathbf{e}}_y$ indicates that buoyancy acts only in the vertical direction. The unknowns are $\mathbf{u} = (u, v)$, p and $\theta = (T - T_H)/(T_H - T_C)$, being the non-dimensional velocity, pressure, and temperature, respectively. These governing equations are obtained by non-dimensionalizing with vertical spacing H between the isothermal walls, free-fall velocity $\sqrt{g\beta\Delta TH}$ and temperature difference between the hot (T_H) and cold (T_C) plates $\Delta T = T_H - T_C$ as length, velocity and temperature scales, respectively.

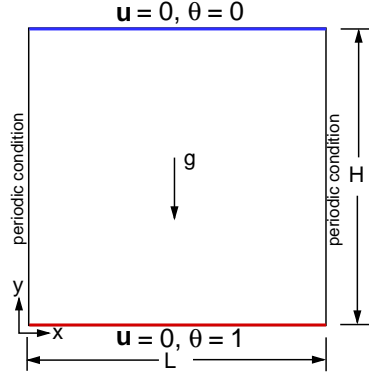


Figure 1: Schematic of a 2D RBC case with boundary conditions.

Case	Ra	$N_x \times N_y$	Δt	$\Delta x/\eta$	N_{BL}	T_{sampling}	NoS
Steady state	10^4	48×48	10^{-2}	0.26	10	[0, 200]	20000
Periodic flow	3×10^5	80×80	10^{-2}	0.49	8	[0, 100]	10000
Chaotic flow	6×10^6	128×128	10^{-2}	0.79	6	[0, 50]	5000

Table 1: Simulation details. From left to right: cases, Ra is Rayleigh number; $N_x \times N_y$ are grid points in x and y directions, respectively, Δt is time increment, $\Delta x/\eta$ is ratio of maximum grid spacing to the Kolmogorov length scale ($\eta = HPr^{1/2}/(\text{Ra}(\text{Nu} - 1))^{1/4}$); N_{BL} is number of grid points inside thermal boundary layer; T_{sampling} is the temporal sampling interval; NoS is number of snapshots used to construct ROM basis.

In this study, we use a 2D square domain filled with air as a working fluid ($\text{Pr} = 0.71$). As shown in Fig. 1, isothermal temperature and no-slip boundary conditions are prescribed on the top and bottom walls, whereas periodic boundary conditions are used for the side walls. To resolve the spatial scales of flow, we ensure that the grid spacing remains smaller than the Kolmogorov length scale [27] and that sufficient number of grid points constitute the boundary layer [28], see Table 1.

2.2. Discrete governing equations and validation

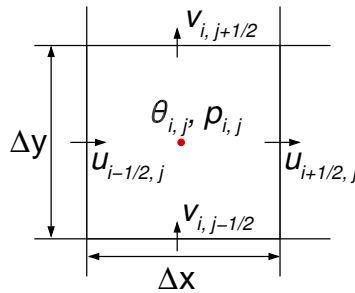


Figure 2: Schematic of a 2D finite volume cell $p_{i,j}$ showing the location of velocity, pressure, and temperature.

The governing equations (1)-(3) are spatially discretized using a staggered grid finite-volume method, yielding the full-order model (FOM) that will be used to construct a reduced-order model in Section 3. Figure 2 shows a schematic of a ‘pressure’ finite volume cell, where velocities are defined on the cell faces and pressure and temperature at the cell centre. A uniform Cartesian grid is used for all the cases. This framework has been used in our earlier work to construct stable ROMs for isothermal cases, see [26]. The discretized veloc-

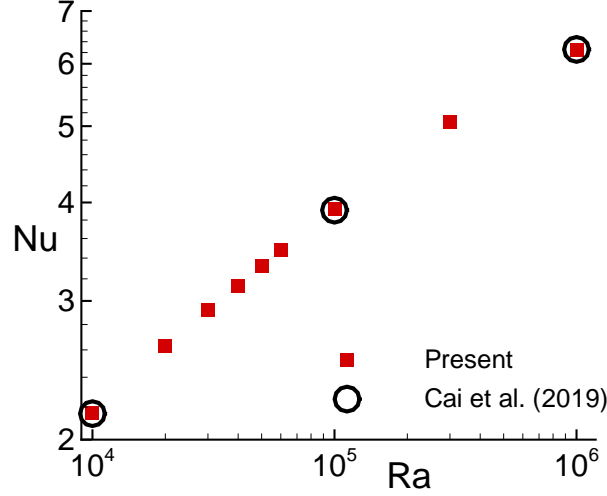


Figure 3: Steady state RBC in a closed cavity: comparison of Nu obtained with our FOM to results of [22].

ity, pressure, and temperature unknowns are represented by $V_h = \begin{pmatrix} u_h \\ v_h \end{pmatrix}$, p_h , and θ_h , respectively. Note that u_h (horizontal velocity) $\in \mathbb{R}^{N_u}$, v_h (vertical velocity) $\in \mathbb{R}^{N_v}$, $p_h \in \mathbb{R}^{N_p}$, and $\theta_h \in \mathbb{R}^{N_\theta}$, where N_u , N_v , N_p , and N_θ represent the number of finite volume cells for the unknowns mentioned in the subscript. The discretized governing equations are written as

$$MV_h(t) = 0, \quad (4)$$

$$\Omega_V \frac{dV_h(t)}{dt} = -C_V(V_h(t)) - Gp_h(t) + \sqrt{\frac{\text{Pr}}{\text{Ra}}} D_V V_h(t) + (A\theta_h(t) + y_A), \quad (5)$$

$$\Omega_\theta \frac{d\theta_h(t)}{dt} = -C_\theta(V_h(t), \theta_h(t)) + \frac{1}{\sqrt{\text{PrRa}}} (D_\theta \theta_h(t) + y_D). \quad (6)$$

$\Omega_V \in \mathbb{R}^{N_v \times N_v}$ and $\Omega_\theta \in \mathbb{R}^{N_\theta \times N_\theta}$ are diagonal matrices whose entries are the finite volume sizes of the velocity and temperature cells, respectively. $M \in \mathbb{R}^{N_p \times N_v}$ indicates the discretized divergence operator, $G = -M^T$ the discretized gradient operator, C_V and C_θ are the (bilinear) convection operators, D_V and D_θ the (linear) diffusion operators, A is an averaging operator (from temperature locations to velocity locations), and y_A and y_D represent boundary condition contributions. For details, see [29].

The discretized governing Eqs. (4)-(6) are solved using a fourth order explicit-Runge Kutta method, where at each stage the velocity is made divergence-free through the solution of a Poisson equation. For details, see [30].

To establish the correct implementation of the FOM, we show a comparison of the Nusselt number Nu (computed on the bottom plate) between the present work and [22] in Fig. 3, for a range of Rayleigh numbers at which steady solutions exist. Note that the comparison is for the case of solid (no-slip) side walls, instead of the periodic ones that will be used in the time-dependent studies. For periodic boundaries, simulations become unstable (periodic or chaotic) already at lower Rayleigh numbers, as will be shown in Section 4. In Fig. 3, Nu refers to the heat flux at the bottom plate, which is defined as

$$\text{Nu} = - \int_0^L \frac{\partial \theta}{\partial y} \Big|_{y=0} dx, \quad (7)$$

where L represent the length of the domain. Nu is one of the key response parameters in RBC [3, 11] and is widely used to validate the numerical setup in RBC [11, 31]. As shown in Fig. 3, Nu computed in the present work is in excellent agreement with the previous study [22]; see also our results in [29].

2.3. Stability and energy conservation

The choice of discrete operators plays a key role in ensuring stable-reduced order modelling [26]. In particular, the staggered-grid method presented in the previous section has three important properties that will make it suitable as a starting point for constructing a reduced-order model.

The first property is that the pressure gradient term does not change the global kinetic energy $\int |\mathbf{u}|^2$ of the system. The pressure gradient contribution in the kinetic energy equation can be written as

$$\int_{\Omega} \nabla p \cdot \mathbf{u} \, d\Omega = \int_{\partial\Omega} p \mathbf{u} \cdot \mathbf{n} \, dS - \int_{\Omega} p \nabla \cdot \mathbf{u} \, d\Omega = 0, \quad (8)$$

assuming periodic or no-slip boundary conditions and $\nabla \cdot \mathbf{u} = 0$. Our FOM inherits this property in a discrete sense:

$$V_h^T (G p_h) = -V_h^T M^T p_h = -(M V_h)^T p_h = 0, \quad (9)$$

because of the fact that the divergence and gradient operator satisfy the compatibility relation $M = -G^T$ on a staggered grid.

The second property is that the convective operator is a skew-symmetric operator that does not change the global kinetic energy of the system. For the continuous equations, the convective contribution to the kinetic energy equation is

$$\int_{\Omega} \nabla \cdot (\mathbf{u} \otimes \mathbf{u}) \cdot \mathbf{u} \, d\Omega = \int_{\partial\Omega} \frac{1}{2} \|\mathbf{u}\|^2 \mathbf{u} \cdot \mathbf{n} \, dS + \int_{\Omega} \frac{1}{2} \|\mathbf{u}\|^2 \nabla \cdot \mathbf{u} \, d\Omega = 0. \quad (10)$$

Again, the FOM inherits this property. This is most easily seen by writing the convective discretization $C_V(V_h)$ as $\tilde{C}_V(V_h)V_h$ [26], where \tilde{C}_V is a skew-symmetric convective operator meaning that $\tilde{C}_V(V_h) = -\tilde{C}_V(V_h)^T$, so that we have

$$V_h^T C_V(V_h) = 0, \quad (11)$$

provided that $M V_h = 0$ and that no-slip and/or periodic boundary conditions hold.

The third property is essentially the same as the skew-symmetry property of the convective operator in the momentum equation, but then for the convective operator in the temperature equation. The continuous equations indicate that the evolution of $\int \theta^2$ should not be changed through convection, since

$$\int_{\Omega} \nabla \cdot (\mathbf{u}\theta)\theta \, d\Omega = \int_{\partial\Omega} \frac{1}{2} \theta^2 \mathbf{u} \cdot \mathbf{n} \, dS + \int_{\Omega} \frac{1}{2} \theta^2 \nabla \cdot \mathbf{u} \, d\Omega = 0. \quad (12)$$

The FOM convective operator $C_{\theta}(V_h, \theta_h)$ satisfies this property, which follows again by writing it in the skew-symmetric form $\tilde{C}_{\theta}(V_h)\theta_h$, with $\tilde{C}_{\theta}(V_h) = -\tilde{C}_{\theta}(V_h)^T$ so that we have

$$\theta_h^T C_{\theta}(V_h, \theta_h) = 0, \quad (13)$$

provided that $M V_h = 0$ and that no-slip and/or periodic boundary conditions apply for the velocity field (for details, see [29]).

3. Novel reduced-order model for natural convection flow

3.1. POD-Galerkin ROM

In constructing a reduced-order model (ROM) for equations (4)-(6) we follow the approach for the incompressible Navier-Stokes equations presented in [26], but extended to include the temperature equation. The velocity field $V_h(t) \in \mathbb{R}^{N_V}$ is approximated by

$$V_h(t) \approx V_r(t) := \Phi a(t), \quad (14)$$

where $\Phi \in \mathbb{R}^{N_V \times M_V}$ is the POD velocity basis, $a(t) \in \mathbb{R}^M$ are the time-dependent velocity coefficients, and $M_V \ll N_V$. In addition to the velocity, we approximate the temperature field $\theta_h(t) \in \mathbb{R}^{N_D}$ by

$$\theta_h(t) \approx \theta_r(t) := \Psi b(t), \quad (15)$$

where $\Psi \in \mathbb{R}^{N_D \times M_\theta}$ is the POD temperature basis, $b(t) \in \mathbb{R}^{M_\theta}$ are the time-dependent temperature coefficients, and $M_\theta \ll N_D$. In the test cases in Section 4, we will take $M_V = M_\theta = M^1$.

Equations (14)-(15) are substituted into the FOM equations (4)-(6), and then the equations are projected by left-multiplying with Φ^T (momentum) and Ψ^T (temperature). Φ and Ψ are obtained by performing a singular-value decomposition (SVD) of snapshot matrices of velocity and temperature, such that the orthogonality conditions

$$\Phi^T \Omega_V \Phi = I, \quad \Psi^T \Omega_\theta \Psi = I, \quad (16)$$

are satisfied. The procedure to construct such bases is described in [26].

This yields the ROM system of equations:

$$\frac{da(t)}{dt} = -\hat{C}_V(a(t) \otimes a(t)) + \sqrt{\frac{\text{Pr}}{\text{Ra}}} \hat{D}_V a(t) + (\hat{A}b(t) + \hat{y}_A), \quad (17)$$

$$\frac{db(t)}{dt} = -\hat{C}_\theta(a(t) \otimes b(t)) + \frac{1}{\sqrt{\text{Pr Ra}}} (\hat{D}_\theta b(t) + \hat{y}_D). \quad (18)$$

The diffusion and buoyancy terms are linear and the associated ROM terms are easily pre-computed from $\hat{D}_V = \Phi^T D_V \Phi$, $\hat{D}_\theta = \Psi^T D_\theta \Psi$ and $\hat{A} = \Phi^T A \Psi$. Similarly, the boundary conditions are naturally included by the projection of the boundary vectors: $\hat{y}_A = \Phi^T y_A$, $\hat{y}_D = \Psi^T y_D$. The convective operators \hat{C}_V and \hat{C}_θ are third-order tensors and are precomputed exactly (as alternative, one can employ energy-conserving hyper-reduction techniques such as [32]). It is important to stress that the divergence-free constraint, equation (4), has disappeared in the ROM formulation. This is because the snapshots of the velocity are divergence-free and consequently the basis Φ is divergence-free. In addition, because of the compatibility relation $G = -M^T$, we have $\Phi^T G = -(\Phi M)^T = 0$, so the pressure gradient term in the momentum equation disappears. As a result, the ROM is pressure-free.

The system of equations (17) - (18) is integrated in time with the same fourth order explicit Runge-Kutta method that was used for the FOM, with the exception that no pressure Poisson equation needs to be solved, since the pressure has disappeared from the ROM formulation.

3.2. Stability and energy conservation

Our proposed ROM formulation (17)-(18) has favorable stability characteristics as it mimics the three properties listed for the FOM in Section 2.3: (i) kinetic-energy conserving pressure gradient, (ii) skew-symmetric momentum convection and (iii) skew-symmetric temperature convection. The first property is trivial to proof because the pressure gradient has disappeared from the formulation. It gives the ROM formulation a strong sense of stability, since any potential issues with inf-sup stability are avoided.

Secondly, the skew-symmetry of the convective terms in the momentum equations is retained upon POD-Galerkin projection: if $\tilde{C}_V(\cdot) = -\tilde{C}_V^T(\cdot)$, then

$$\Phi^T \tilde{C}_V(\Phi a) \Phi = -\Phi^T \tilde{C}_V(\Phi a)^T \Phi = -(\Phi^T \tilde{C}_V(\Phi a) \Phi)^T, \quad (19)$$

which is still skew-symmetric, and the contribution to the kinetic energy equation is

$$a^T \Phi^T \tilde{C}_V(\Phi a) \Phi a = 0, \quad (20)$$

just like for the FOM and for the continuous equations. Thirdly, the skew-symmetry of the convective terms in the temperature equation is also retained upon POD-Galerkin projection: if $\tilde{C}_\theta = -\tilde{C}_\theta^T$, then

$$\Psi^T \tilde{C}_\theta(\Phi a) \Psi = -\Psi^T \tilde{C}_\theta(\Phi a)^T \Psi = -(\Psi^T \tilde{C}_\theta(\Phi a) \Psi)^T, \quad (21)$$

¹from the context the distinction between the number of modes M and the discrete divergence operator M should be clear

which is still skew-symmetric, and its contribution to the equation for the ROM approximation to θ^2 is

$$b^T \Psi^T \tilde{C}_\theta(\Phi a) \Psi b = 0, \quad (22)$$

just like equation (13).

Overall, the fact that the skew-symmetric nature of the convective terms is retained by our ROM, combined with the fact that it is pressure-free, makes it suitable for long-time integration, which is necessary in RBC in order to sample statistics.

4. Results

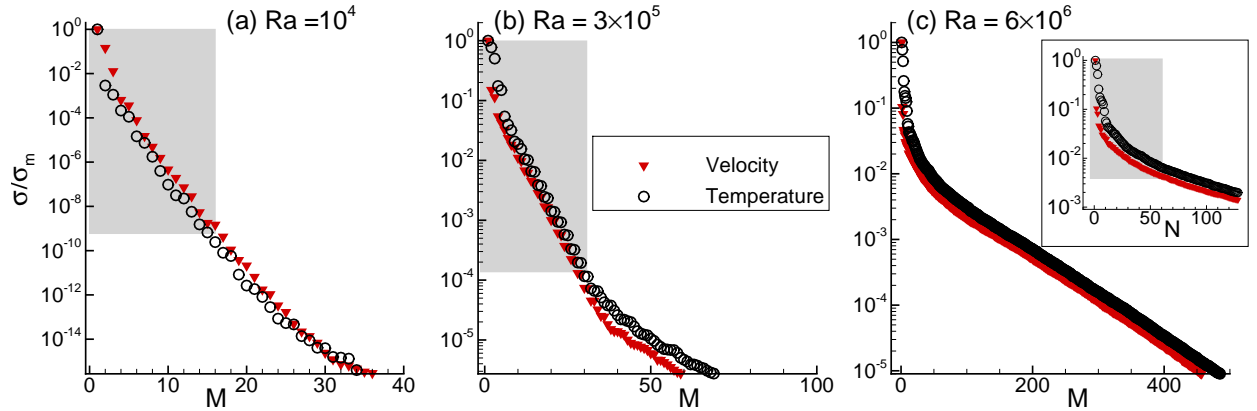


Figure 4: Decay of singular values (σ/σ_m) with increasing modes (M) for (a) $Ra = 10^4$, (b) 3×10^5 , and (c) 6×10^6 . Here, σ_m refers to the maximum singular value; the shaded region indicates the maximum number of modes ($M = 16, 32$ and 64 in (a), (b) and (c), respectively) used in the three Ra cases.

In this section, we discuss the long-time stability and accuracy of the proposed ROM for the three cases that were listed in Table 1. The reason for studying these cases lies in their different flow dynamics, ranging from steady state (time-independent) to chaotic. For all the FOM cases, we ensure that the grid resolution remains smaller than the Kolmogorov length scale ($\Delta x/\eta < 1$) and that a sufficient number of grid points constitute the thermal boundary layer (N_{BL}). We propose to use the mean ($\langle \theta \rangle$) and variance (σ_θ) of the temperature as a measure of the ROM accuracy, defined as

$$\langle \theta \rangle(y) = \langle \theta \rangle_{A,t} \quad \text{and} \quad \sigma_\theta(y) = \langle (\theta - \langle \theta \rangle_t)^2 \rangle_{A,t} \quad (23)$$

where $\langle \cdot \rangle_{A,t}$ represents averaging in x -direction and in time. These profiles reveal the physical characteristic of the flow. For instance, they both are a measure of thermal boundary layer thickness and characterize the bulk and boundary layer region [3, 33, 11]. Convergence of the variance, being a second-order statistic, is more difficult than convergence in the mean (a first-order statistic), even for the FOM. Requiring convergence of second-order statistics for the ROM is therefore a good and stringent test to assess its accuracy.

In addition, we use two global heat transport properties (Nu and Re) to investigate the ROM's stability and accuracy. In contrast to temperature mean and variance, these are still a function of time (but not of space). While Nu is given by Eq. (7), Re can be defined as

$$Re(t) = \sqrt{\frac{Ra}{Pr} \langle \mathbf{u} \cdot \mathbf{u} \rangle_V}, \quad (24)$$

where $\langle \cdot \rangle_V$ refers to volume averaging. These two quantities are the primary objective of any RBC study.

Before starting the discussion of the results, we first describe the decay of the singular values in the three cases, see Fig. 4. The singular values (with respect to weighted inner product) represent the kinetic energy of

the system. The singular value decay helps in the selection of the number of modes required to approximate the FOM, where the selection process is solely based on capturing the total kinetic energy. It is apparent that $M = 16, 32,$ and 64 modes are sufficient to capture at least 99% of the kinetic energy in $Ra = 10^4, 3 \times 10^5$ and 6×10^6 , respectively, see the shaded region. The singular values are computed by performing an SVD of the snapshot matrix. It is important to mention that the snapshot matrix is constructed from the start of the simulation ($t = 0$) for the steady state case, whereas, for the other two cases, it is constructed after attaining the statistical steady state, see T_{sampling} in Table 1. This state begins once the flow passes the transient period, and it is identified by stable Nu and Re time series.

Note that in the results presented here we are not reporting the computational speed-up achieved by the ROM compared to the FOM, as we focus on the stability and accuracy properties of the method. However, as the ROM proposed here is an extension of the ROM proposed in [26], we can expect very similar speed-ups. For example, with $M = 8$ the speed-up in that work was $\mathcal{O}(10^3)$.

4.1. Steady flow case

We start the discussion by studying the time series parameters Nu and Re. Figure 5a shows the Nu time series for different cases: (i) the FOM, (ii) the FOM with initial condition as the best approximation solution (FOM_{BIC}), and (iii) the ROM with different number of modes. Figure 5a shows that the evolution of Nu time series is different in all the cases. Figure 5b shows a similar result, but displaying Re instead of Nu. The difference between the cases is remarkable, given that the difference between the exact initial condition and its best approximation is of order 10^{-14} . This minimal difference in the initial condition triggers a slightly early onset to convection. A similar behavior can be noted for the ROM cases: the fewer the number of modes, the earlier is the onset to convection. This indicates that simulations that are chaotic (highly sensitive to initial conditions or parameter values) can yield rather different results even for a very small perturbation, as caused for example by the approximation of the FOM by the ROM. Consequently, in order to assess the accuracy of the ROM it is important to use error metrics that involve averaging in time, like equation (23).

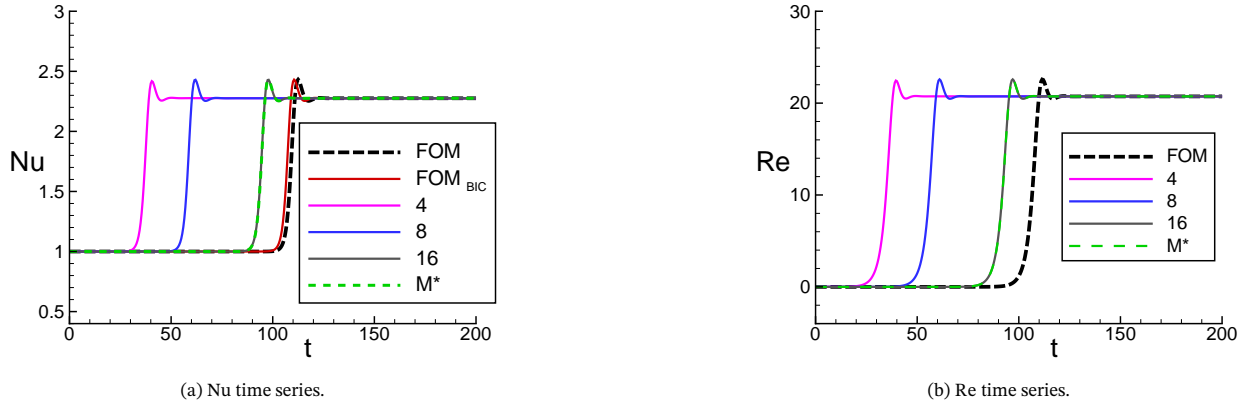


Figure 5: Effect of initial condition and M on the onset of convection at $Ra = 10^4$. Here FOM_{BIC} refers to the FOM case whose initial condition is the best approximation computed by considering all the modes ($M^* = 4560$).

In order to further clarify this point, we split the error in the ROM solution that employs all modes ($M = M^*$) as

$$V_r^n - V_h^n = \underbrace{V_r^n - V_{\text{best}}^n}_{\text{temporal error}} + \underbrace{V_{\text{best}}^n - V_h^n}_{\text{basis error due to SVD precision}}, \quad (25)$$

where $V_{\text{best}}^n = \phi\phi^T \Omega_h V_h^n$. We define the errors

$$L_2^V = \frac{\|V_r^n - V_h^n\|_{\Omega_h}}{\|V_{\text{ref}}\|_{\Omega_h}} \quad \text{and} \quad \epsilon_{\text{best}}^V = \frac{\|V_{\text{best}}^n - V_h^n\|_{\Omega_h}}{\|V_{\text{ref}}\|_{\Omega_h}}, \quad (26)$$

where V_{ref} and $\|\cdot\|_{\Omega_h}$ represent a reference velocity and the Ω_h norm, respectively. Figure 6 shows a comparison of the evolution of the error in the ROM velocity field (L_2^V) when all modes are included (4560 in total), and the best approximation (ϵ_{best}^V). The best approximation error is at machine precision. The L_2^V error also starts with a magnitude of order of machine precision but grows significantly (owing to a horizontal shift in the large-scale structure due to early onset of convection). In view of equation (25), this means that the temporal error $V_r^n - V_{\text{best}}^n$ is dominating the evolution of L_2^V . Therefore, comparing the L_2^V and ϵ_{best}^V errors does not give a good measure of the accuracy of the ROM. This is in contrast to what was concluded for a non-chaotic system in [26].

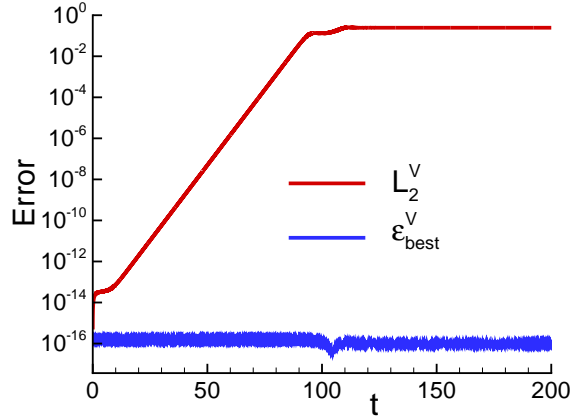


Figure 6: Comparison between evolution of error in ROM velocity with all the modes $M^* = 4560$ (L_2^V) and error obtained by projecting FOM velocity field onto the POD modes (ϵ_{best}^V), see text for their definition.

Instead, to assess the ROM accuracy in chaotic flows, we propose to employ statistical quantities, namely the first two moments (mean and variance) of the temperature as defined in equation (23). In Fig. 7, the effect of M on the vertical profiles of mean and variance of temperature is shown. In comparison to the Nu and Re time series, clearer convergence is obtained in the vertical profiles of mean temperature, where the ROM profiles shift towards that of the FOM as M increases. Furthermore, the vertical profiles of the variance indicate that the temperature statistics obtained with the ROM also converges upon increasing M . The profiles nearly overlap with the FOM data when all the modes are considered. To elucidate this, in Fig. 7, we quantify the error in the ROM profiles as

$$S = \frac{|\sigma_{\theta_{\text{FOM}}} - \sigma_{\theta_{\text{ROM}}}|}{|\sigma_{\theta_{\text{FOM}}}|} \times 100. \quad (27)$$

These profiles clearly show diminishing errors with increasing number of modes. In particular, for $M \geq 16$, the error drops below 2%. Only a slight difference close to the top wall is observed.

Note that the relatively large errors for $M = 4$ and $M = 8$ are mainly due to the difference in onset time (see figure 5a). As was shown, this difference in onset time persists even for $M = M^*$, due to the chaotic nature of the system, and consequently a small error remains in the vertical profiles even for $M = M^*$. If one would time-average over only the last few time units, then the profiles would be very close, as only the best approximation error would remain.

Lastly, we show why it is important to perform horizontal averaging. Fig. 8 shows the mean temperature field for different numbers of modes. As expected, flow features appear nearly similar in all the cases because they capture more than 99% of kinetic energy. However, a horizontal offset in the field is evident which can be attributed to a slightly different onset of convection in combination with periodic boundary conditions in lateral direction. Upon horizontal averaging, such effects do not influence the error computation negatively.

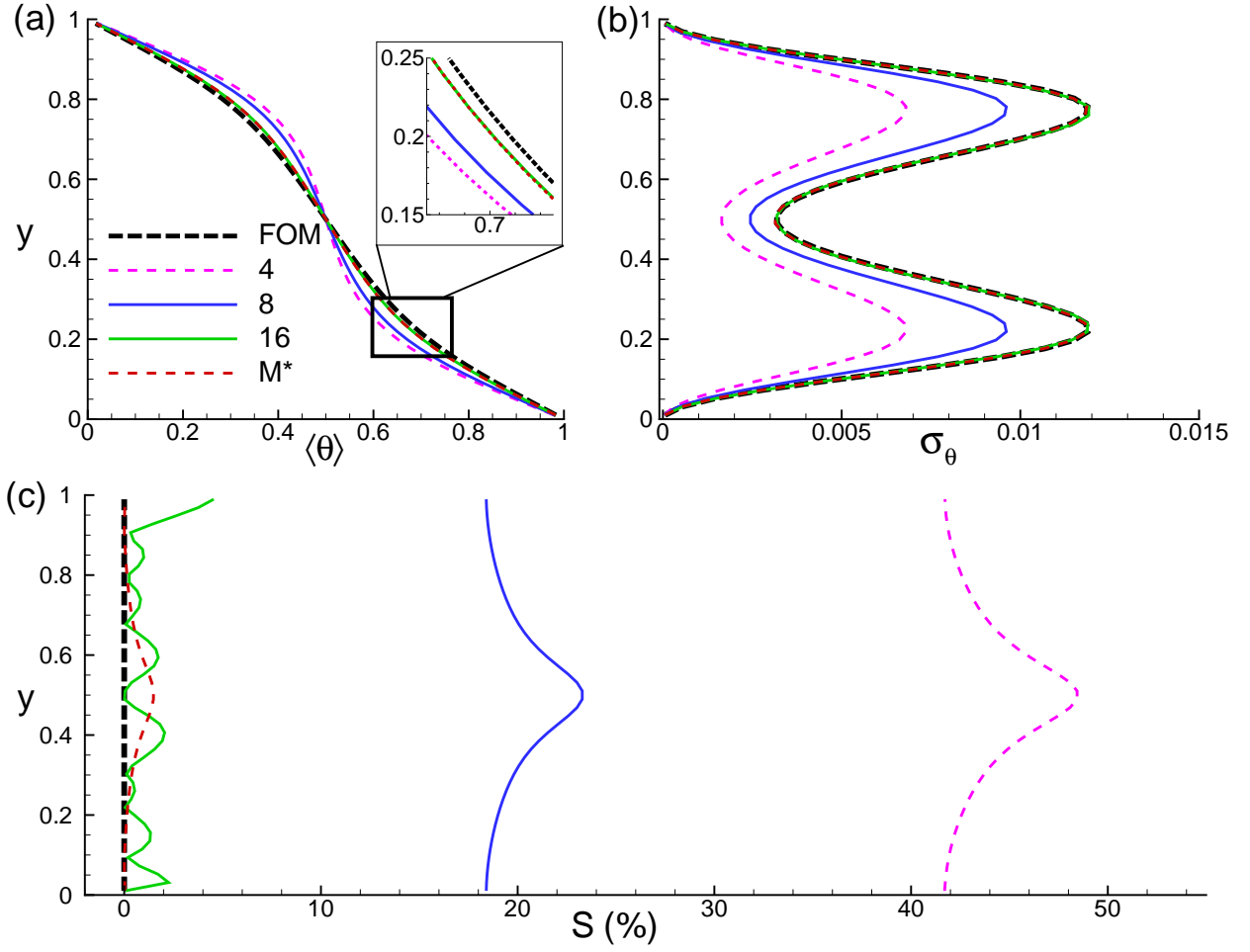


Figure 7: Vertical profiles of mean and variance of temperature for $Ra = 10^4$.

M	Nu			Re		
	Mean ($\langle Nu \rangle_t$)	$Nu_{\text{error}}(\%)$	Amplitude (range)	Mean ($\langle Re \rangle_t$)	$Re_{\text{error}}(\%)$	Amplitude (range)
FOM	5.17	0.00	4.75 – 5.5	180.64	0.00	175.5 – 185.5
4	9.47	83.17	3.19 – 15.74	220.05	21.82	81.04 – 359.05
8	5.00	3.29	4.85 – 5.45	180.81	0.09	175.5 – 186.5
16	5.18	0.19	4.75 – 5.5	180.37	0.15	175.5 – 186.5
32	5.17	0.00	4.75 – 5.5	180.63	0.01	175.5 – 186.5

Table 2: Nu and Re comparison for $Ra = 3 \times 10^5$. From left to right: Modes; time average heat flux $\langle Nu \rangle_t$; error in $\langle Nu \rangle_t$ ($Nu_{\text{error}} = |(1 - \langle Nu_{\text{ROM}} \rangle_t) / \langle Nu_{\text{FOM}} \rangle_t| \times 100$); range of Nu; time average Reynolds number $\langle Re \rangle_t$; error in $\langle Re \rangle_t$ ($Re_{\text{error}} = |(1 - \langle Re_{\text{ROM}} \rangle_t) / \langle Re_{\text{FOM}} \rangle_t| \times 100$); and range of Re.

4.2. Periodic flow case

Next, we discuss the periodic flow case at $Ra = 3 \times 10^5$. We first investigate again the convergence of the ROM through Nu and Re time series and then through the statistics of the temperature. Note that 100 time units of the FOM are used to build the snapshot matrix (and corresponding basis), which is subsequently used to run the ROM for 600 time units (effectively extrapolating in time). Figure 9 shows the Nu time series. All ROM cases

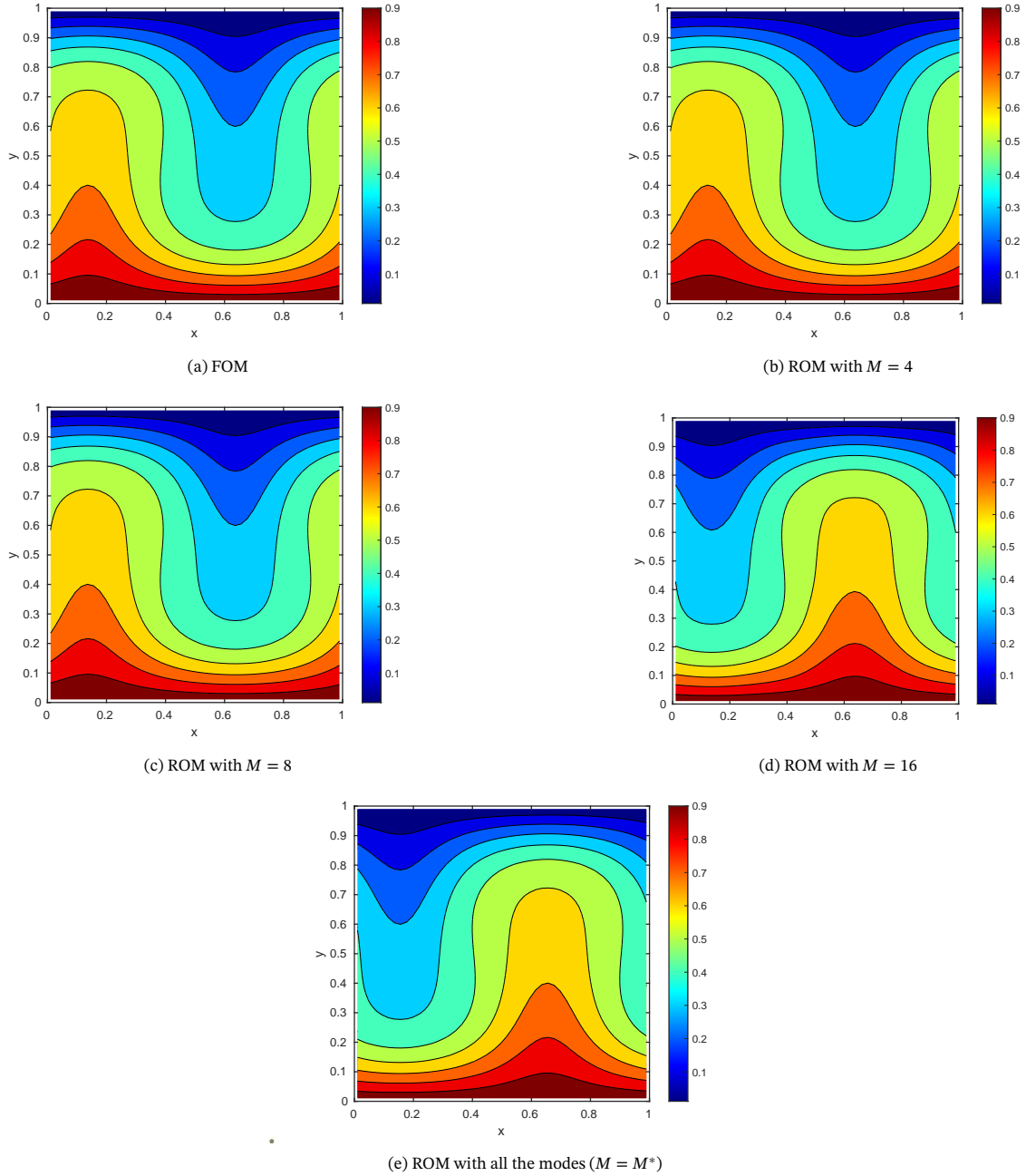


Figure 8: Comparison of instantaneous temperature field of the last time instance for $Ra = 10^4$.

yield a periodic Nu time series, see zoomed-view (Frame b) for higher modes ($M > 4$). It is observed that the Nu series with $M = 4$ deviates significantly from the FOM, which can be attributed to the lower amount of energy captured by these few modes, see Fig. 4b. Compared to the previous test case ($Ra = 10^4$), this can be attributed to the fact that the singular value decay is much slower. Importantly, even with such a low number of modes, the solution stays stable when marching in time, without requiring any stabilization mechanism. When the ROM simulation is still inside the training interval $[0, 100]$, we see clear convergence towards the FOM solution upon increasing the number of modes. Outside the training interval, point-wise convergence in time is lost, but the

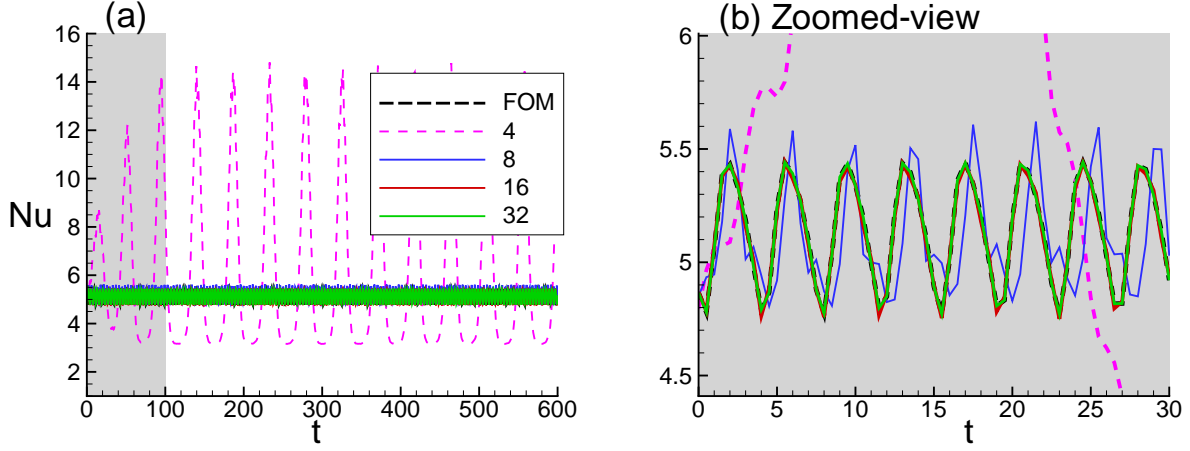


Figure 9: (a) Nu time series for $Ra = 3 \times 10^5$. (b) Zoomed-view of the time series shown in (a). The grey shaded region indicates the data used to compute POD basis from FOM.

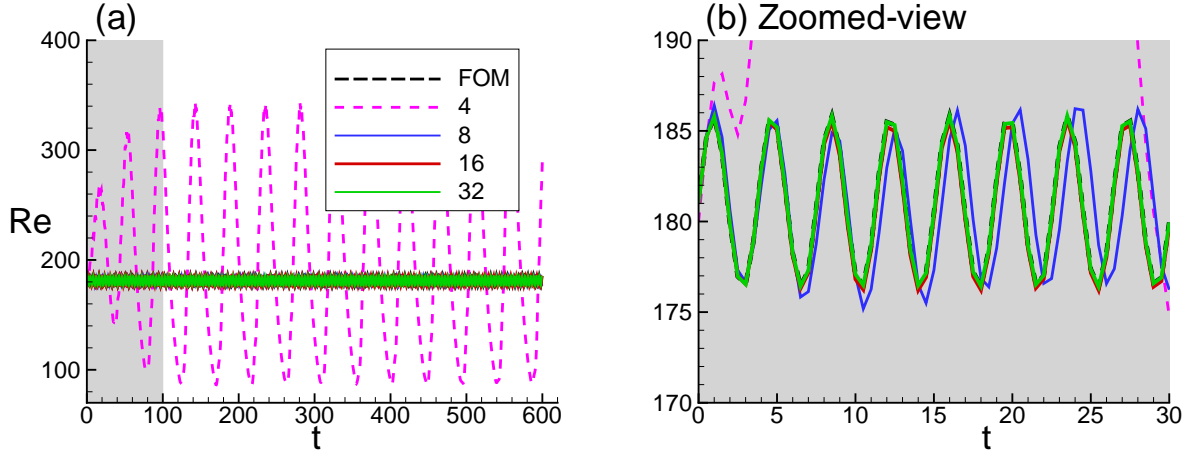


Figure 10: (a) Re time series for $Ra = 3 \times 10^5$. (b) Zoomed-view of the time series shown in (a). The grey shaded region indicates the data used to compute POD basis from FOM.

amplitude of the oscillations of the ROM still converges to that of the FOM upon increasing the number of modes. To elucidate this, we show the range of the amplitude of oscillations and the corresponding mean values for both Nu and Re in Table 2. It is evident that with increasing M , the mean value approaches the value of the FOM. Similar results are reflected from the Re time series, see Fig. 10. The mean Re for the FOM and the ROM with $M = 32$ are nearly equal, and the range of amplitude is also similar beyond $M = 8$. The error drops below 1% beyond $M = 8$.

Figure 11 compares the effect of M on the statistics of the temperature. Roughly, the vertical profiles of $\langle \theta \rangle$ of all the ROM cases (except for $M = 4$) overlap with those of the FOM. Moreover, the vertical profiles of the variance show a clear convergence, see the inset in Fig. 11b, where the ROM profiles shift towards that of the FOM as M increases. The convergence is further confirmed by a diminishing relative error S , which is less than 5% beyond $M = 4$ in almost the entire domain. In comparison with the previous (steady flow) test case, we observe again that the main dynamics and statistics are correctly captured even though the time series of the FOM are not exactly reproduced in a point-wise sense.

Figure 12 shows the mean temperature field for the FOM and the ROM cases. A periodic finger-like structure is evident in all the cases. In the smallest mode case, the structures appear to be more elongated as compared

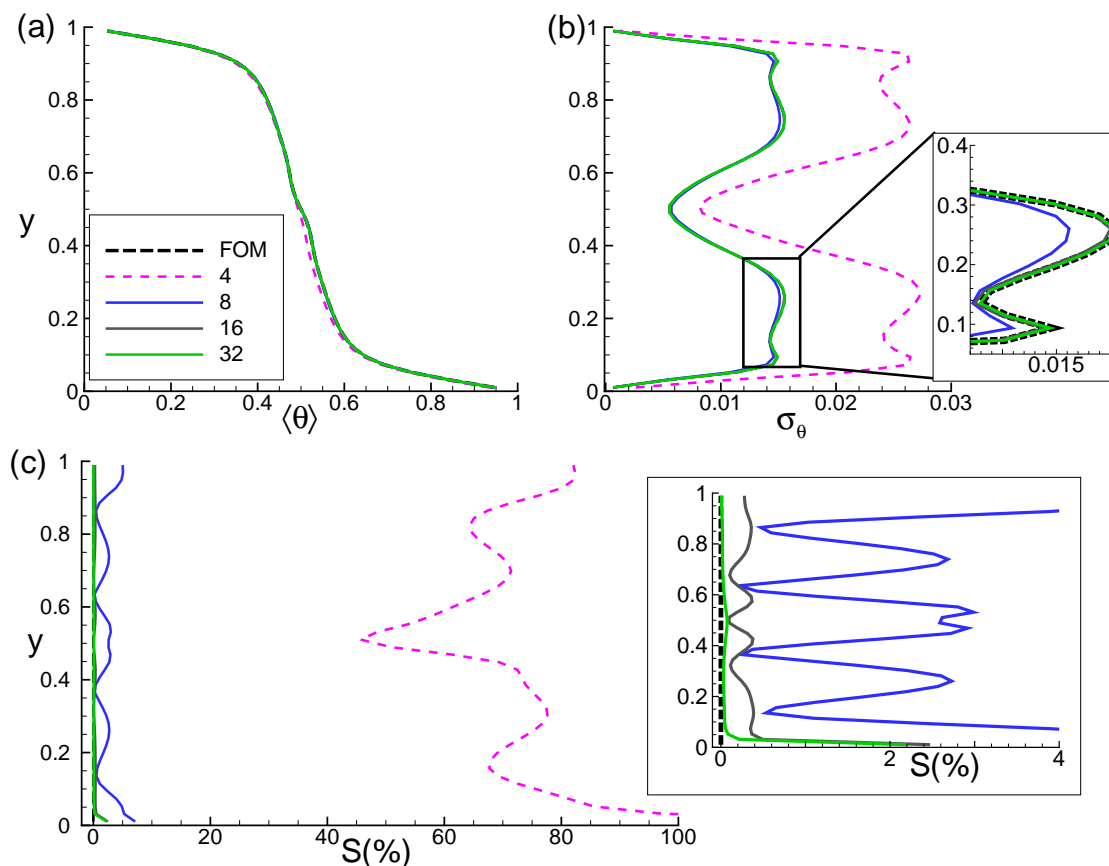


Figure 11: For $Ra = 3 \times 10^5$, vertical profiles of (a) mean temperature $\langle \theta \rangle$, (b) variance of temperature σ_θ , and (c) relative error (S) in the ROM profiles of σ_θ with respect to the FOM. Insets show the zoomed-view.

to other higher modes and FOM cases. Moreover, the near-wall regions seem relatively more disturbed. These variations can be attributed to the fact that insufficient kinetic energy is captured by the ROM with $M = 4$ (see Fig. 4). Fortunately, when more modes are included, the flow structures in the ROM closely resemble those of the FOM, and already at $M = 16$ the mean field looks visually indistinguishable. Note that the horizontal shift that was observed in Fig. 8 is not present in this simulation.

4.3. Chaotic flow case

We finally investigate the convergence of the ROM for a chaotic case ($Ra = 6 \times 10^6$). This case typifies turbulent flow characteristics and we again discuss accuracy and stability of the ROM. Figures 13 and 14 show the evolution of Nu and Re , respectively. Contrary to the previous case, neither the Nu nor the Re time series obtained with the FOM show clear periodic characteristics, which justifies the reason for selecting this case.

Our first observation is that our ROM yields a stable solution and corresponding time series for Nu and Re , independent of the number of modes chosen. Note that only 50 time units were used for constructing the snapshot matrix, whereas the ROM is simulated much longer in time, namely until 400 time units. Also in this extrapolation scenario, our proposed ROM yields stable results.

However, in contrast to the periodic flow case, a qualitative inspection shows that the time series do *not* indicate a clear trend with increasing number of modes, even when simulating within the training period. In order to make this more quantitative, we compute the mean global transport properties and their relative error, see Table 3. The relative error is roughly around 10% for $M \geq 8$, in both Nu and Re . The table confirms that convergence of the error with increasing number of modes is not apparent.

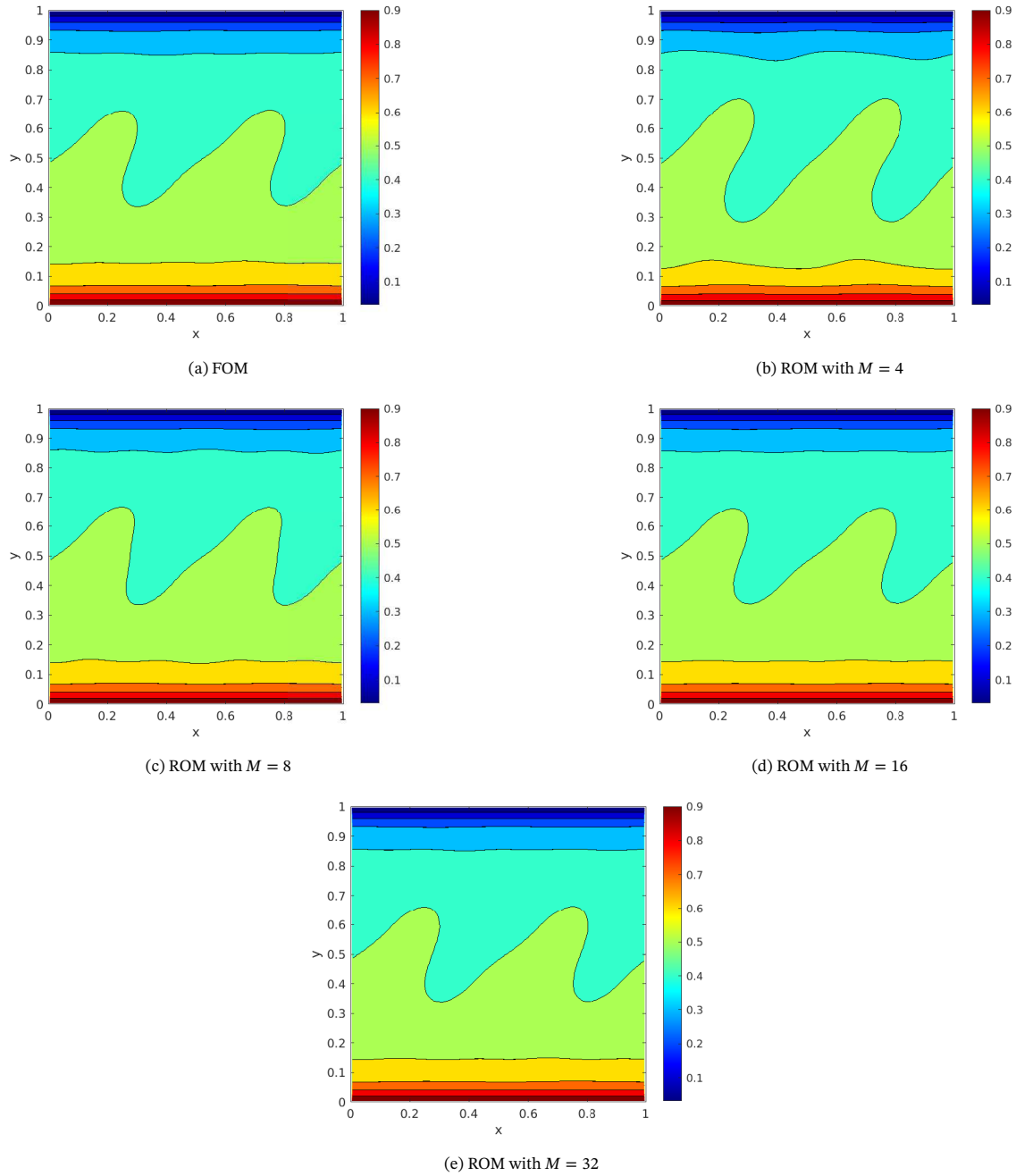


Figure 12: Comparison of mean temperature field for $Ra = 3 \times 10^5$. The averaging is carried out over 550 time units.

We continue to study the temperature statistics in terms of vertical profiles of mean and variance, see Fig. 15. In line with the observations for the Nu and Re time series, the variance profiles do not show clear convergence with increasing number of modes. For example, the relative error does not converge at certain vertical locations, for instance around $y = 0.8$, where the $M = 64$ case has a larger error than the $M = 48$ case. On the other hand, the mean temperature profile shows quite clear convergence with increasing number of modes, which is probably due to the fact that it is a ‘simpler’ quantity of interest than the other ones, which involve the temperature gradient

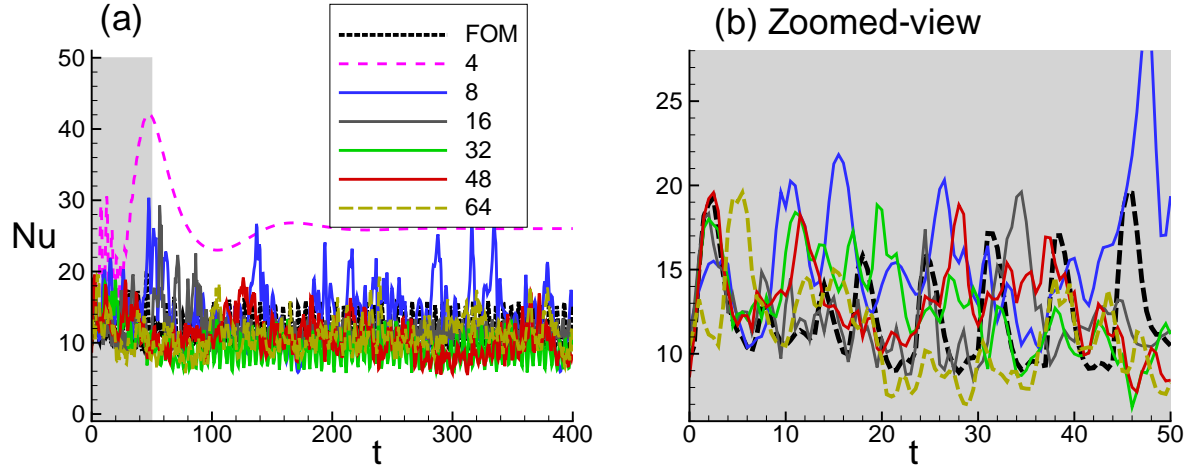


Figure 13: (a) Nu time series for $Ra = 6 \times 10^6$. (b) Zoomed-view of the time series shown in (a). The grey shaded region indicates the data used to compute POD basis from FOM.

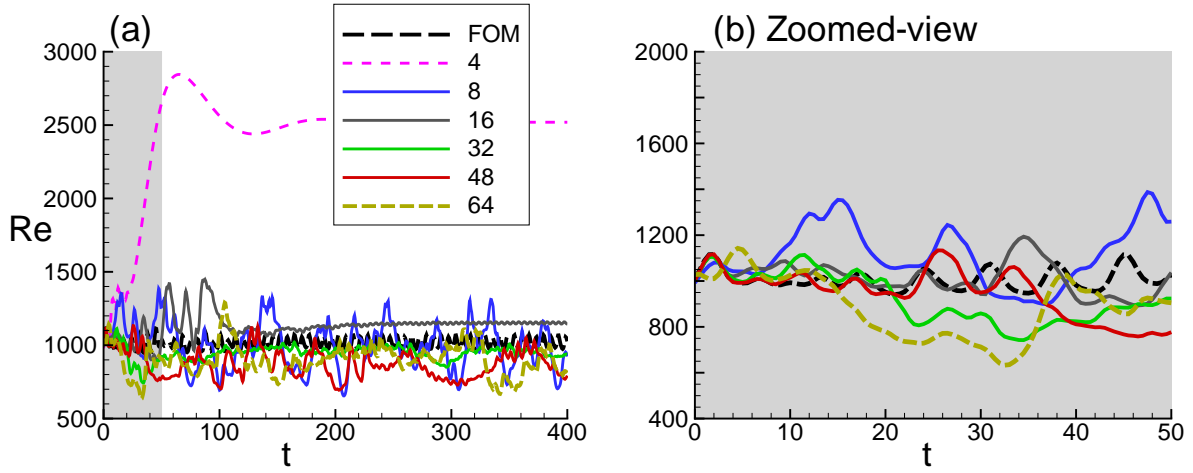


Figure 14: (a) Re time series for $Ra = 6 \times 10^6$. (b) Zoomed-view of the time series shown in (a). The grey shaded region indicates the data used to compute POD basis from FOM.

Modes (M)	Nu		Re	
	$\langle Nu \rangle_t$	$Nu_{\text{error}}(\%)$	$\langle Re \rangle_t$	$Re_{\text{error}}(\%)$
FOM	11.608	0.00	1012.603	0.00
4	26.687	129.88	1667.52	64.67
8	15.71	35.30	1113.59	9.97
16	12.23	5.34	1014.01	0.14
32	12.80	10.29	922.96	8.85
48	12.99	11.87	949.92	6.19
64	11.09	4.45	888.69	12.24

Table 3: Nu and Re comparison for $Ra = 6 \times 10^6$. From left to right: Modes; time average heat flux $\langle Nu \rangle_t$; error in $\langle Nu \rangle_t$ ($Nu_{\text{error}} = |(1 - \langle Nu_{\text{ROM}} \rangle_t / \langle Nu_{\text{FOM}} \rangle_t)| \times 100$); time average Reynolds number $\langle Re \rangle_t$; and error in $\langle Re \rangle_t$ ($Re_{\text{error}} = |(1 - \langle Re_{\text{ROM}} \rangle_t / \langle Re_{\text{FOM}} \rangle_t)| \times 100$).

or a second-order statistic. In conclusion: it is clearly much more difficult to achieve the same level of ROM accuracy in the chaotic case compared to the cases at lower Ra (steady state and periodic case). This is further confirmed by the mean temperature fields in Fig. 16.

At first sight, not observing convergence might seem counter-intuitive, given the fact that in all cases the ROM basis contains more than 99% of the energy, and consequently the best approximation errors will be small enough. However, the process of dissipation, which is highly important in turbulent flows, happens at scales that carry hardly any energy. Such scales will therefore always be missed by a ROM based on POD (which ranks modes in terms of energy), except when a very large number of modes is included, which would however defeat the very purpose of model reduction. Consequently, the delicate balance between energy production, convection and dissipation cannot be accurately represented by the ROM. This is a known issue, see e.g. [21, 23], which surfaces here in the study of turbulent natural convection flow. One possible solution is to add a closure model to the ROM equations, like in [22]. Our proposed framework, which is stable even without including such a closure model, could form an ideal testbed for developing such closure models.

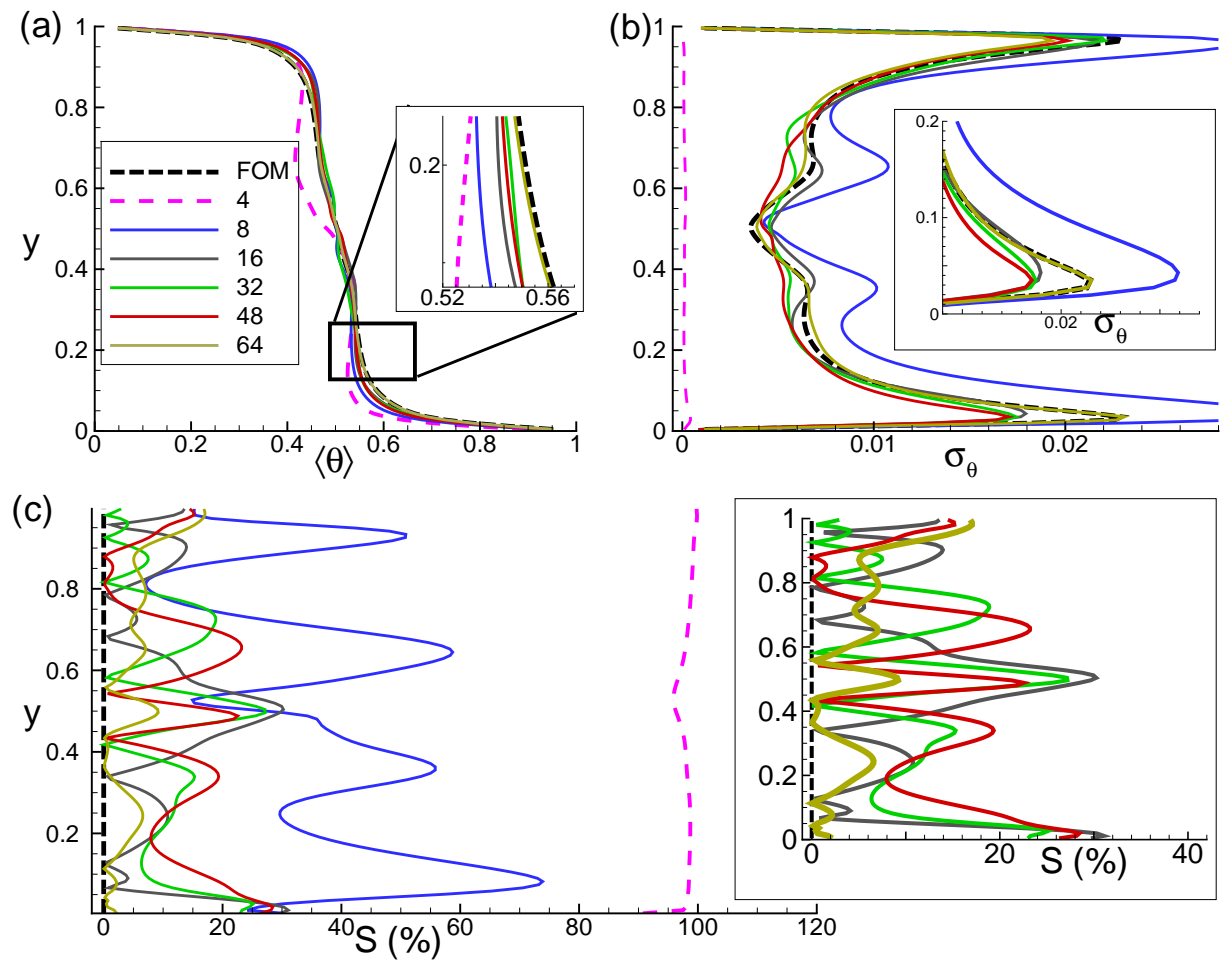


Figure 15: For $Ra = 6 \times 10^6$, vertical profiles of (a) mean temperature $\langle \theta \rangle$, (b) variance of temperature σ_θ , and (c) relative error (S) in the ROM profiles of σ_θ with respect to the FOM. Insets show the zoomed-view.

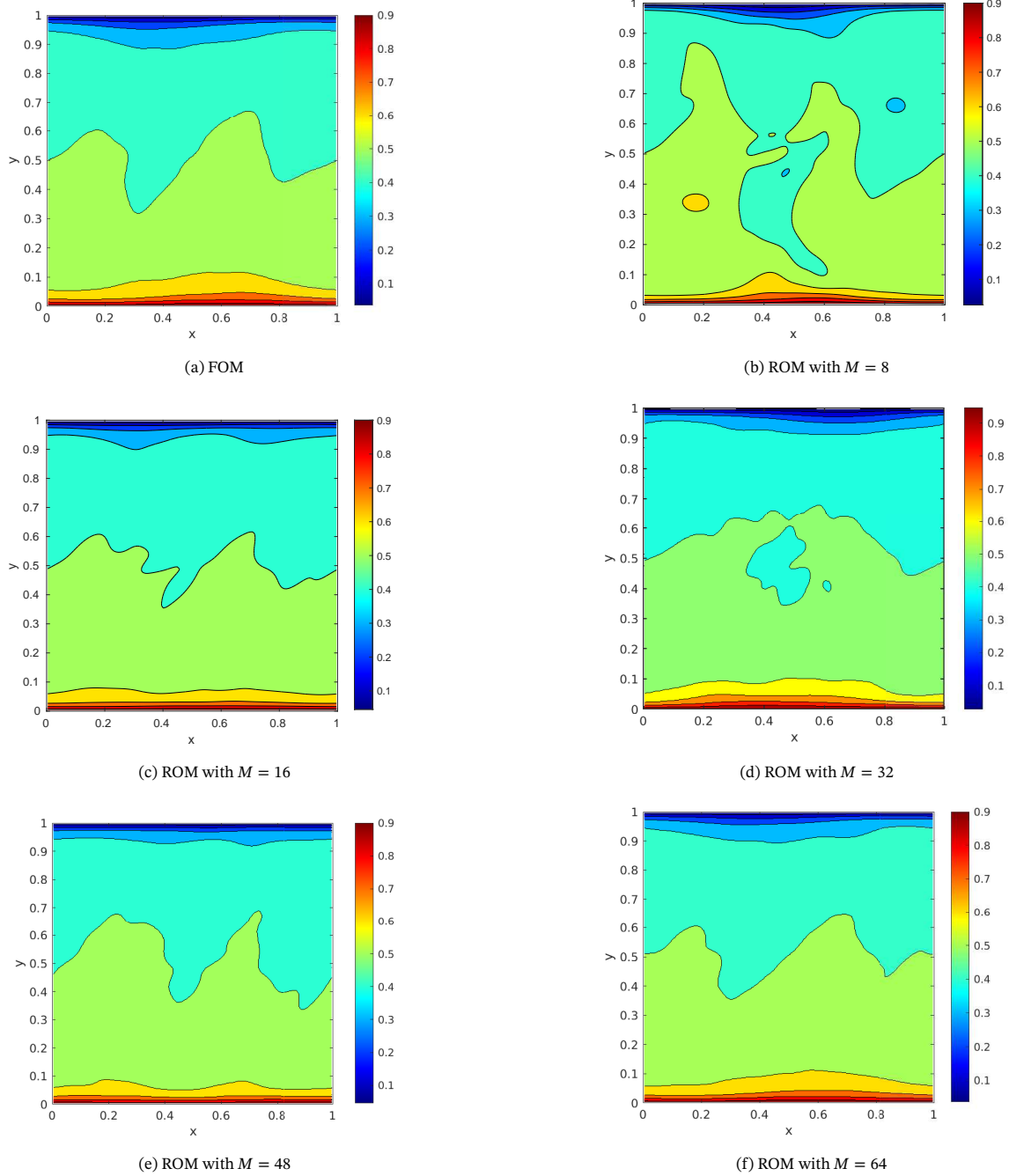


Figure 16: Comparison of mean temperature field for $Ra = 6 \times 10^6$. The averaging is carried out for 350 time units.

5. Conclusions

In the present work, a pressure-free, long-time stable reduced-order model (ROM) is proposed for 2D Rayleigh-Bénard convection (RBC). The POD-Galerkin ROM is constructed with a ‘discretize-first, project-later’ approach. The discretization on a staggered grid ensures compatibility of the gradient and divergence operators, skew-symmetry of the convective operators (both in momentum transport and temperature transport), and symmetry

of the diffusive operators. Upon projection, this results in a pressure-free ROM model that does not suffer from inf-sup stability issues, does not have spurious energy production from the convective terms, and consequently forms an excellent starting point for long-time sampling of statistics in natural convection problems.

In this study, the following control parameters are used: $Pr = 0.71$; $Ra = 10^4$, 3×10^5 , and 6×10^6 ; and a square box with periodic boundary conditions across the lateral walls. The three Ra cases refer to steady state (10^4), periodic (3×10^5) and chaotic (6×10^6) cases. Given the sensitivity of the flow dynamics to the initial conditions, two time-independent measures have been used to assess the accuracy of ROMs, i.e., the mean and variance of the vertical temperature profiles. In addition, a comparison of the time-dependent global heat transport properties (Nu and Re) is carried out to investigate the accuracy and long-time flow stability. The main observations can be summarized as:

- With increasing Ra , the singular-value decay becomes much slower. This can be attributed to the growing importance of the convective motion and the presence of smaller scales.
- For all cases, the ROMs are stable far beyond their training interval.
- For the steady state and periodic flows: increasing the number of modes yields good convergence, where the relative error between FOM and ROM is below 0.2% in terms of the Nu - and Re -time series for $M = 16$ modes, and below 2% in terms of the mean and variance profiles for $M = 32$ modes.
- For the chaotic flow case: the mean temperature profile shows relatively good convergence with increasing modes, but the Nu and Re time-series and the variance profile do not show clear convergence. This is attributed to the presence of small scale structures, which carry little energy, but are important for the overall energy balance and amount of dissipation.

In summary, the present work has provided a ROM framework to carry out stable long-time sampling in turbulent RBC, which is of great importance to understand heat transport in turbulent natural convection flows. The stable nature of the framework forms an excellent starting point to improve its accuracy with closure models that represent the effect of the smallest scales.

Data Availability Statement

The incompressible Navier-Stokes code is available at <https://github.com/bsanderse/INS2D> (Matlab version). A Julia version (without ROM capability) is available from <https://github.com/agdestein/IncompressibleNavierStokes>. The data generated in this work is available upon request.

CRediT authorship contribution statement

K. Chand: Methodology, Software, Writing - Original Draft, Investigation, Visualization; **H. Rosenberger:** Methodology, Software, Writing - Review & Editing, Supervision; **B. Sanderse:** Conceptualization, Software, Writing - Original Draft, Writing - Review & Editing, Supervision, Funding acquisition, Project administration

Acknowledgements

This publication is part of the project "Discretize first, reduce next" (with project number VI.Vidi.193.105 of the research programme NWO Talent Programme Vidi which is (partly) financed by the Dutch Research Council (NWO)).

References

- [1] H. Bénard, Les tourbillons cellulaires dans une nappe liquide. -Méthodes optiques d'observation et d'enregistrement, *Journal de Physique Théorique* 10 (1901) 254–266.
- [2] L. Rayleigh, On convection currents in a horizontal layer of fluid, when the higher temperature is on the under side, *Philosophical Magazine and Journal of Science: Series 6* 32 (1916) 529–546.
- [3] G. Ahlers, S. Grossmann, D. Lohse, Heat transfer and large scale dynamics in turbulent Rayleigh-Bénard convection, *Rev. Mod. Phys.* 81 (2009) 503–537.
- [4] F. Chilla, J. Schumacher, New perspectives in turbulent Rayleigh-Bénard convection, *Eur. Phys. J. E.* 35 (2012) 58.
- [5] X. Zhu, R. J. A. M. Stevens, R. Verzicco, D. Lohse, Roughness facilitated local $1/2$ scaling does not imply the onset of the ultimate regime of thermal convection, *Phys. Rev. Lett.* 119 (2017) 154501.
- [6] X. Zhu, V. Mathai, R. J. A. M. Stevens, R. Verzicco, D. Lohse, Transition to the ultimate regime in two-dimensional Rayleigh-Bénard convection, *Phys. Rev. Lett.* 120 (2018) 144502.
- [7] W. V. R. Malkus, S. Chandrasekhar, The heat transport and spectrum of thermal turbulence, *Proceedings of the Royal Society of London. Series A. Mathematical and Physical Sciences* 225 (1161) (1954) 196–212. doi : 10.1098/rspa.1954.0197.
- [8] R. H. Kraichnan, Turbulent thermal convection at arbitrary Prandtl number, *Phys. Fluids* 5 (1962) 1374.
- [9] S. Grossmann, D. Lohse, Scaling in thermal convection: a unifying theory, *J. Fluid Mech.* 407 (2000) 27–56.
- [10] Q. Zhou, K. Xia, Physical and geometrical properties of thermal plumes in turbulent Rayleigh-Bénard convection, *New J. Phys.* 12 (2010) 075006.
- [11] K. Chand, M. Sharma, V. T. Venugopal, A. K. De, Statistics of coherent structures in two-dimensional turbulent Rayleigh-Bénard convection, *Physics of Fluids* 31 (11) (2019) 115112. doi : 10.1063/1.5125758.
- [12] D. Lohse, K.-Q. Xia, Small-scale properties of turbulent Rayleigh-Bénard convection, *Annual Review of Fluid Mechanics* 42 (1) (2010) 335–364. doi : 10.1146/annurev.fluid.010908.165152.
- [13] Q. Wang, S. Xia, B. Wang, D. Sun, Q. Zhou, Z. Wan, Flow reversals in two-dimensional thermal convection in tilted cells, *J. Fluid Mech.* 849 (2018a) 355–372.
- [14] M. S. Emran, J. Schumacher, Conditional statistics of thermal dissipation rate in turbulent Rayleigh-Bénard convection, *Eur. Phys. J. E.* 35 (2012) 108.
- [15] C. Schneide, A. Pandey, K. Padberg-Gehle, J. Schumacher, Probing turbulent superstructures in Rayleigh-Bénard convection by Lagrangian trajectory clusters, *Phys. Rev. Fluids* 3 (2018) 113501. doi : 10.1103/PhysRevFluids.3.113501.
- [16] A. Pandey, Thermal boundary layer structure in low-prandtl-number turbulent convection, *Journal of Fluid Mechanics* 910 (2021) A13. doi : 10.1017/jfm.2020.961.
- [17] S. B. Pope, *Turbulent Flows*, Cambridge University Press, 2000.
- [18] A. C. Antoulas, *Approximation of Large-Scale Dynamical Systems*, Society for Industrial and Applied Mathematics, 2005. doi : 10.1137/1.9780898718713.
- [19] P. Benner, S. Gugercin, K. Willcox, A survey of projection-based model reduction methods for parametric dynamical systems, *SIAM Review* 57 (4) (2015) 483–531. doi : 10.1137/130932715.
- [20] G. Stabile, G. Rozza, Finite volume POD-Galerkin stabilised reduced order methods for the parametrised incompressible Navier-Stokes equations, *Computers & Fluids* 173 (2018) 273–284. doi : https://doi.org/10.1016/j.compfluid.2018.01.035.
- [21] Z. Wang, I. Akhtar, J. Borggaard, T. Iliescu, Proper orthogonal decomposition closure models for turbulent flows: A numerical comparison, *Computer Methods in Applied Mechanics and Engineering* 237-240 (2012) 10–26. doi : https://doi.org/10.1016/j.cma.2012.04.015.
- [22] W. Cai, H. Ma, Y. Wang, J. Chen, X. Zheng, H. Zhang, Development of POD reduced-order model and its closure scheme for 2D Rayleigh-Bénard convection, *Applied Mathematical Modelling* 66 (2019) 562–575. doi : https://doi.org/10.1016/j.apm.2018.09.031.
- [23] S. E. Ahmed, S. Pawar, O. San, A. Rasheed, T. Iliescu, B. R. Noack, On closures for reduced order models—A spectrum of first-principle to machine-learned avenues, *Physics of Fluids* 33 (9) (09 2021). doi : 10.1063/5.0061577.
- [24] A. Iollo, S. Lanteri, J.-A. Désidéri, Stability properties of POD-Galerkin approximations for the compressible Navier-Stokes equations, *Theoretical and Computational Fluid Dynamics* 13 (2000) 377–396.
- [25] K. Carlberg, Y. Choi, S. Sargsyan, Conservative model reduction for finite-volume models, *Journal of Computational Physics* 371 (2018) 280–314. doi : https://doi.org/10.1016/j.jcp.2018.05.019.
- [26] B. Sanderse, Non-linearly stable reduced-order models for incompressible flow with energy-conserving finite volume methods, *Journal of Computational Physics* 421 (2020) 109736. doi : https://doi.org/10.1016/j.jcp.2020.109736.
- [27] G. Grötzbach, Spatial resolution requirements for direct numerical simulation of the Rayleigh-Bénard convection, *Journal of Computational Physics* 49 (2) (1983) 241–264. doi : https://doi.org/10.1016/0021-9991(83)90125-0.
- [28] O. Shishkina, R. J. A. M. Stevens, S. Grossmann, D. Lohse, Boundary layer structure in turbulent thermal convection and its consequences for the required numerical resolution, *New Journal of Physics* 12 (7) (2010) 075022. doi : 10.1088/1367-2630/12/7/075022.
- [29] B. Sanderse, F. X. Trias, Energy-consistent discretization of viscous dissipation with application to natural convection flow, *ArXiv preprint 2307.10874* (2023).
- [30] B. Sanderse, B. Koren, Accuracy analysis of explicit Runge-Kutta methods applied to the incompressible Navier-Stokes equations, *Journal of Computational Physics* 231 (8) (2012) 3041–3063. doi : https://doi.org/10.1016/j.jcp.2011.11.028.
- [31] K. Chand, A. K. De, P. K. Mishra, Enhanced heat flux and flow structures in turbulent Rayleigh-Bénard convection with rough boundaries, *Phys. Rev. Fluids* 6 (2021b) 124605. doi : 10.1103/PhysRevFluids.6.124605.
- [32] R. Klein, B. Sanderse, Structure-preserving hyper-reduction and temporal localization for reduced order models of incompressible flows, *ArXiv preprint 2304.09229* (2023).
- [33] Q. Zhou, K. Sugiyama, R. J. A. M. Stevens, S. Grossmann, D. Lohse, K. Xia, Horizontal structures of velocity and temperature boundary layers in two-dimensional numerical turbulent Rayleigh-Bénard convection, *Phys. Fluids* 23 (2011) 125104.